

Article

Pore Structure and Fractal Characteristics of Tight Sandstone: A Case Study for Huagang Formation in the Xihu Sag, East China Sea Basin, China

Jin Dong ^{1,2} , Zhilong Huang ^{2,3,*}, Jinlong Chen ^{2,3}, Tianjun Li ^{2,3}, Jing Zhao ^{2,3}, Yongshuai Pan ^{2,3} and Tong Qu ^{2,3}

¹ Research Institute of Petroleum Exploration and Development, China National Petroleum Corporation, Beijing 100083, China

² College of Geosciences, China University of Petroleum, Beijing 102249, China

³ State Key Laboratory of Petroleum Resource and Prospecting, China University of Petroleum, Beijing 102249, China

* Correspondence: huangzhilong1962@163.com

Abstract: Various experiments, including routine petrophysical measurements, thin section and scanning electronic microscope (SEM), high-pressure mercury intrusion (HPMI), and nuclear magnetic resonance (NMR), were performed to characterize the microscopic pore structure of tight sandstone in the Huagang Formation (E_{3h}), Xihu Sag, East China Sea Basin, China. Specifically, NMR was used to investigate the dynamic variation of fractal dimensions during centrifugation, and the comparison of HPMI and NMR were used to clarify the difference of fractal dimensions. The results showed that there were four types of pores observed in thin section and SEM images: primary intergranular pores, intergranular dissolution pores, intragranular dissolution pores, and micropores within clay aggregates. The geometric shape and pore size of different pore types showed huge differences, indicating the formation of complex and diverse pore structures in the E_{3h} formation. The flow capability of the reservoir was dominated by large pores, while the storage capacity was determined by small pores. The dynamic variation of fractal dimensions calculated by NMR data showed the water residing in the pore structure with low fractal dimensions was removed preferentially, and the pore structure of the resided water was always more complicated than the pore structure of removed water, which indicated the flow capability of the reservoir was affected by the complexity of the pore structure. Based on the comparison of the fractal dimension data from HPMI and NMR, it was found that the variation trends of the fractal dimensions were consistent, as the radius of the pore throat increased, the fractal dimensions increased, and the pore structure became more complicated. Both fractal dimensions of macropores (D_{mac}) and movable-fluid pores (D_{mov}) can reflect the flow capability of reservoir effectively, but the correlations between fractal dimensions from HPMI and NMR were poor, which could be due to the different working mechanism in these methods.



Citation: Dong, J.; Huang, Z.; Chen, J.; Li, T.; Zhao, J.; Pan, Y.; Qu, T. Pore Structure and Fractal Characteristics of Tight Sandstone: A Case Study for Huagang Formation in the Xihu Sag, East China Sea Basin, China. *Energies* **2023**, *16*, 2013. <https://doi.org/10.3390/en16042013>

Academic Editor: Prabir Daripa

Received: 27 August 2022

Revised: 25 January 2023

Accepted: 7 February 2023

Published: 17 February 2023

Keywords: East China Sea Basin; tight sandstone reservoir; pore structure; HPMI; NMR with centrifugation; fractal analysis



Copyright: © 2023 by the authors. Licensee MDPI, Basel, Switzerland. This article is an open access article distributed under the terms and conditions of the Creative Commons Attribution (CC BY) license (<https://creativecommons.org/licenses/by/4.0/>).

1. Introduction

In recent years, the development of tight sandstone gas and oil resources has shown rapid growth and become an important area of exploration and development in China [1,2]. Reservoirs with porosity of < 12% and air permeability ≤ 1 mD are defined as tight sandstones [3,4]. The tight sandstone reservoirs are characterized by the complexity and irregularity of pore throat geometry, poor connectivity, and strong heterogeneity [5]. In tight sandstones, the reservoir quality and hydrocarbon migration are controlled by the microscopic pore structure [6,7]. In order to get an accurate evaluation, the petrophysical

properties and pore structure of tight sandstone reservoirs must be investigated and clarified [8].

The microscopic pore structure, which includes the geometry shape, pore-throat size and distribution, and their connectivity, is an important factor affecting reservoir quality [9]. Various techniques including thin section [10], scanning electronic microscope (SEM) [11,12], high-pressure mercury intrusion (HPMI) [13,14], nuclear magnetic resonance (NMR) [15], and gas adsorption/desorption measurements [16,17] are applied to the characterization of pore structure. Due to the complex geometry of pore structure and wide distribution of pore-throat size, it is difficult to fully characterize the pore structure of tight sandstone by any single technique, so comprehensive research based on multiple technologies is required [18,19]. The fractal theory has been widely used in the characterization of pore structures based on previous studies [14,20,21]. The data of thin section, SEM, HPMI, NMR, and N₂ gas adsorption (N₂GA), which are commonly used to characterize pore structure, can be used to calculate fractal dimensions [21–23]. The complex degree and heterogeneity of pore structure in a reservoir can be quantitatively characterized by calculating fractal dimensions [5], accompanied by microscopic analysis of pore structures to macroscopic properties [24]. Therefore, a comprehensive study based on thin section, SEM, HPMI, NMR, and fractal theory are significant for the research of microscopic pore structures in tight sandstone reservoirs.

The middle-deep sandstones of the Huagang Formation (E₃h) in Xihu Sag, East China Sea Basin, belonging to the category of tight sandstone reservoirs, are important hydrocarbon-producing reservoirs with large exploration potential [25]. It is critical to clarify the petrophysical properties and pore structure of tight sandstone reservoirs for exploration, evaluation, and production [26]; however, research in the area of E₃h reservoirs is rare. The purpose of this study is: (1) to characterize the pore type and pore throat distribution in the E₃h reservoir by thin section, SEM, HPMI, and NMR; (2) to calculate the fractal dimensions from HPMI and NMR data and discuss the complexity and heterogeneity of tight sandstone reservoirs in E₃h; (3) to compare the fractal dimensions from HPMI and NMR to discuss their correlation and difference.

2. Geological Setting

The East China Sea Basin is the largest Meso-Cenozoic petroliferous basin in China offshore, located at the edge of the eastern China continent [25,27]. Xihu Sag is a significant hydrocarbon-producing sag with great exploration potential, located in the northeast of the East China Sea Basin with an area of 59,000 km² (Figure 1) [28]. Xihu sag is closed by the Hupijiao Uplift, Changjiang Sag, Haijiao Uplift, and Yushan Uplift in the west, by the Taiwan-Sinzi Fold Belt in the east, by the Diaobei Sag in the south, and by the Fujiang Sag in the north [29]. Xihu Sag has experienced three tectonic evolution stages: the rifting stage from Paleocene to the end of Eocene, the depression stage from Oligocene to the end of Miocene, and the subsidence stage from Pliocene to present [30]. From the bottom up, the stratigraphy in Xihu sag is Paleocene (E₁), lower Eocene Baoshi Formation (E₂b), upper Eocene Pinghu Formation (E₂p), Oligocene Huagang Formation (E₃h), lower Miocene Longjing Formation (N₁¹l), middle Miocene Yuquan Formation (N₁²y), upper Miocene Liulang Formation (N₁³l), Pliocene Santan Formation (N₂s), and Quaternary Donghai Formation (Qd) (Figure 2). The target formation E₃h is deltaic and lacustrine, with the tight sandstone reservoir as the main component, and it is a significant hydrocarbon reservoir in the Xihu Sag [28,29].

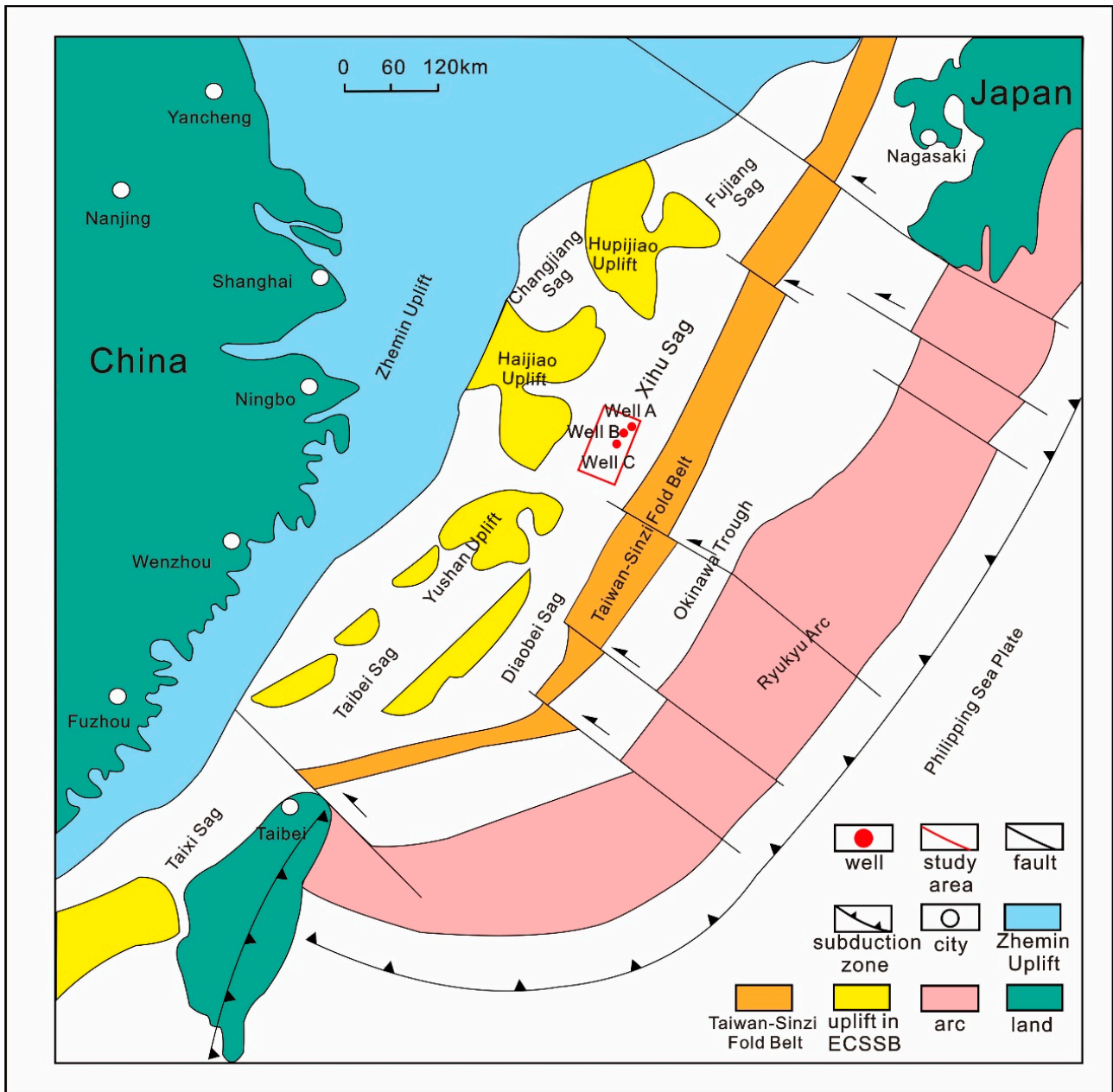


Figure 1. Location map of the study area and tectonic framework of the East China Sea (modified after Hao, 2018).

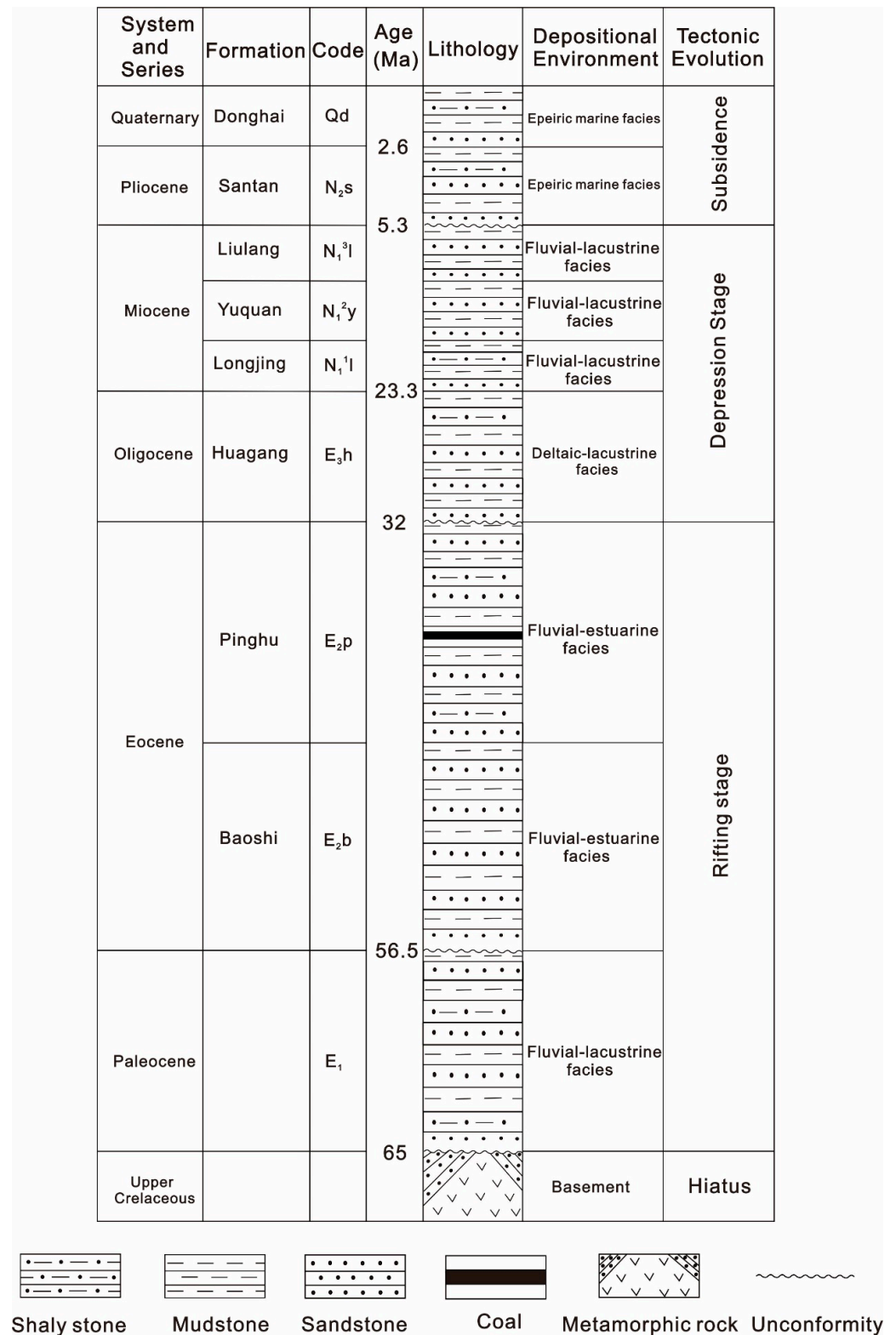


Figure 2. Stratigraphy, deposition, and tectonic evolution in the Xihu Sag (modified after Su 2018).

3. Experiments and Modeling

3.1. Sample and Experiments

Seven samples of E₃h reservoir drill cores were collected from three wells in the Xihu Sag (Table 1). Various experiments including routine petrophysical measurements,

thin section and SEM observation, HPMI, and NMR were performed on the samples to characterize the microscopic pore structure of tight sandstone reservoirs in study areas.

Table 1. Physical properties of seven core samples in Xihu Sag.

Sample	Well	Depth(m)	Formation	Porosity(%)	Permeability(mD)
1	Well A	3600.72	H3	10.84	11.88
2		3961.62	H4	5.13	0.17
3		3980.48	H4	8.61	0.96
4	Well B	3742.45	H3	12.84	23.49
5		3792.35	H3	12.69	54.82
6	Well C	3126.45	H3	15.82	14.29
7		3132.47	H3	16.08	5.37

The data of the porosity and permeability are measured in cylindrical cores with a diameter of 2.5 cm. According to the American Petroleum Institute standard (API RP-40), PoroPDP-200 Pulse decay permeameter is used to measure porosity and permeability.

The morphology of the pore throat can be clarified by the images of thin section and SEM. The thin section is impregnated with blue resin to highlight the pore structure and observed by Leica DMRXHC and Linkam THMSG600 optical microscopes. Pore structures of freshly broken rock fragments with a thin layer of gold were studied by SEM using a scanning electron microscope (FEI Quanta 200 FEG) equipped with an energy-dispersive X-ray spectrometer (OXFORD IE 350).

HPMI is widely used to clarify the characterization of pore throat structure [31]. Mercury (non-wetting phase) was injected into samples by increasing pressure to overcome the capillary pressure. The amount of mercury in the equilibrium state under different pressures was recorded to obtain a capillary pressure curve. Pore-throat radius can be calculated corresponding to capillary pressure by Equation (1) [32], and the amount of mercury injected into the samples represents the volume of the throat and its connected pore. Therefore, the pore throat structure can be characterized by a capillary pressure curve [5,14]. The surface tension of air/mercury is 485 mN/m, and the wetting angle is 140° in Equation (1).

$$P_c = \frac{2\sigma \cos\theta}{r} \quad (1)$$

where P_c is the capillary pressure (MPa), σ is the surface tension, θ is the contact angle (°), and r is the pore-throat radius (μm). Seven samples underwent HPMI analysis using an AutoPore III 9505 pore size analyzer. The maximum intrusion pressure was 200.33 MPa, corresponding to a pore-throat radius of 3.7 nm.

NMR is a technology to detect the pore structure by measuring the amplitude and relaxation rate of the nuclear magnetic resonance relaxation signal of the hydrogen nuclei in the pore fluid, based on the principle of interaction between the magnetic properties of the hydrogen nuclei and the applied magnetic field [33,34]. In NMR measurements, the spin axis relaxation times of protons are recorded in the presence of pulsed and static magnetic fields [33]. There are three relaxation mechanisms in the NMR measurements: bulk fluid processes, surface interactions, and diffusion in internal field gradients, and this multiexponential process can be expressed in Equation (2)

$$\frac{1}{T_2} = \frac{1}{T_{2B}} + \frac{1}{T_{2D}} + \frac{1}{T_{2S}} \quad (2)$$

where T_2 is the transverse relaxation time, T_{2B} , T_{2D} , and T_{2S} are the bulk relaxation time (ms), diffusion-induced relaxation time (ms), and surface relaxation time (ms), respectively. When short TE is used and the pores are saturated with water only, T_{2S} plays a major role, and T_2 is directly proportional to the pore size [34,35].

$$\frac{1}{T_2} \approx \frac{1}{T_{2S}} = \rho \left(\frac{S}{V} \right) \quad (3)$$

where ρ is the transverse surface relaxivity strength ($\mu\text{m}/\text{s}$), S is the pore surface area (μm^2), and V is the pore volume (μm^3). Then, S/V can be converted into a function of pore radius r and pore shape factor a to obtain Equation (4) [15].

$$\frac{1}{T_2} = \rho \left(\frac{a}{r} \right) \quad (4)$$

Therefore, the longer T_2 relaxation time corresponds to a larger pore size, whereas the small pore size was represented by a shorter T_2 relaxation time, through which way the pore size distribution of reservoir can be characterized by the T_2 spectrum [19]. The specific experimental conditions and parameters include the resonance frequency set as 12.80 MHz, the magnet strength set as 0.301 T, the coil diameter of 25 mm, the magnet temperature of 32 °C; the time of echo (TE) of 0.15 ms, and the echo number of 16,000. The SIRT algorithm is adopted in this paper, and the number of inversions is selected to be 200. After measuring the water-saturated NMR, the samples were centrifuged at 1000 r/min for 30 min, with the corresponding capillary pressure of about 8.71 psi, and the T_2 distributions were also measured. Then, in the same way, the samples were further centrifuged at 2000 r/min (34.84 psi) and 3000 r/min (78.38 psi) and measured for T_2 distributions. The centrifugal NMR data can be used to distinguish bounded-fluid pores and moveable-fluid pores.

3.2. Fractal Analysis Methods

Fractal has been applied widely in various fields and is defined as self-similar objects which are identical independent of the scale of magnification, and these fractal objects could be characterized by the fractal dimension D_f or D [36–38]. Previous research has confirmed the fractal features of complex pore structures in reservoirs [20,21]. According to the work of Pfeifer and Avnir (1983), the number of elements N showed a power law relationship with the element's length scale r in a fractal structure (Equation (5)) [39].

$$N(r) = C r^{-D_f} \quad (5)$$

where C is the constant of proportionality and D is the fractal dimension. Previous studies have provided a number of methods to calculate fractal dimensions, which can be based on experiments including thin section, SEM, HPMI, NMR, and N_2 GA [14,21,22]. In this paper, the data of HPMI and NMR were used to calculate the fractal dimensions of pore structure in E_3h reservoirs from Xihu Sag.

3.2.1. Fractal Analysis Method from HPMI

Assuming that the pore space consists of bundles of capillary tubes, the number of pores with a pore size larger than r can be expressed by Equation (6) [40].

$$N(r) = \frac{V(r)}{\pi r^2 l} \quad (6)$$

where $V(r)$ is the pore volume in a fixed radius, r is the pore radius, and l is the length of a capillary tube. Assuming $r = 1$ and combining Equations (5) and (6) with integral transformation, we obtain Equation (7).

$$\frac{dV(r)}{dr} = C(3 - D)\pi r^{2-D} \quad (7)$$

Obtaining the integral formula of cumulative pore volume with pore radius less than r (Equation (8)).

$$V(< r) = \int_{r_{min}}^r C(3 - D)\pi r^{2-D} dr = C\pi(r^{3-D} - r_{min}^{3-D}) \quad (8)$$

According to Equation (7), the formula of cumulative pore volume fraction f_r can be obtained (Equation (9)).

$$f_r = \frac{V(< r)}{V(< r_{max})} = \frac{r^{3-D} - r_{min}^{3-D}}{r_{max}^{3-D} - r_{min}^{3-D}} \quad (9)$$

where r_{min} and r_{max} are the minimum and maximum pore radius. Since r_{min} is much smaller than r and r_{max} , Equation (9) can be simplified to Equation (10).

$$f_r = \frac{r^{3-D}}{r_{max}^{3-D}} \quad (10)$$

Combining Equations (10) and (1) to obtain Equation (11).

$$f_r = \frac{V(< r)}{V(< r_{max})} = \left(\frac{P_c}{P_{cmin}} \right)^{D-3} \quad (11)$$

f_r represents the volume fraction of the wetting phase which is replaced by the non-wetting phase [40]. Substituting formula of $S_{Hg} = 1 - f_r$ into Equation (11), and taking the logarithm to both sides of equation to obtain Equation (12)

$$\log(1 - S_{Hg}) = (D - 3)\log P_c - (D - 3)\log P_s \quad (12)$$

Based on Equation (12), by the linear relationship of $\log(1 - S_{Hg})$ and $\log(P_c)$, the fractal dimension D can be calculated from the slope.

3.2.2. Fractal Analysis Method from NMR

According to the theory of NMR, the pore radius r can be converted into T_2 spectrum. Therefore, Equation (10) can be converted into Equation (13).

$$f_r = \left(\frac{T_2}{T_{2max}} \right)^{3-D} \quad (13)$$

where T_{2max} is the maximum transverse relaxation time. Taking the logarithm to both sides of Equation (13) to obtain Equation (14).

$$\log(f_r) = (3 - D)\log(T_2) + (D - 3)\log(T_{2max}) \quad (14)$$

The fractal dimension D can be calculated by the slope of the regression line in the intersection figure of $\log(f_r)$ and $\log(T_2)$. We can use this method to calculate the fractal dimension of the water saturated NMR core, after centrifugation, and the difference between different centrifugal speeds.

4. Results and Discussion

4.1. Physical Properties and Pore Types

Table 1 shows the information of pore and permeability from routine petrophysical measurements. The porosity of the samples ranged from 5.13% to 16.08% with an average of 11.72%, whereas the permeability ranged from 0.17 mD to 54.82 mD with an average of 15.85 mD. Positive correlation exists between porosity and permeability with a correlation coefficient of 0.57 (Figure 3).

The casting thin section and SEM observation indicated four types of pores dominating the tight sandstone reservoirs in E₃h: primary intergranular pores, intergranular dissolution pores, intragranular dissolution pores, and micropores within clay aggregates. The primary intergranular pores were mainly residual pores remaining from compaction and cementation during the burial process, and they were mostly triangular or irregu-

lar polygons with diameters ranging from 3 to 150 μm (Figure 4A–C). The intergranular dissolution pores were mainly derived from feldspar dissolution, and were mostly harbor-shaped or crescent-shaped, with diameters less than 100 μm (Figure 4A,B). The dissolution of feldspar along the cleavage direction formed the intragranular dissolution pores, and most of the diameters were less than 20 μm with poor connectivity (Figure 4B,D). Micropores within clay aggregates developed in authigenic clay minerals (including chlorite, kaolinite, illite, and mixed illite/smectite layers), which were distributed on the surface of grains or filled in the intergranular pores. Micropores within clay aggregates were widely developed in the reservoirs of E_{3h} with complex structure and poor connectivity, and their diameters are generally less than 10 μm (Figure 4E,F). The pores of different types vary in shape (e.g., irregular polygons or crescent pores) and size (10–100 μm). Most of the pore throats were sheet-like or bending-flake-like, showing effects on the flow capacity of the reservoir (Figure 4B).

4.2. Pore Throat Network Characteristics from HPMI

HPMI experiments are widely used to measure pore-throat size distribution and connectivity of the reservoir, which can give information such as maximum pore-throat radius, average pore-throat radius, entry pressure, median saturation pressure, and maximum mercury saturation [24]. Table 2 shows the HPMI parameters for the samples of the E_{3h} reservoir. The maximum pore-throat radius showed a wide range from 1.1 to 21.37 μm and an average of 8.78 μm . The average pore-throat radius ranged from 0.22 to 6.28 μm with an average of 2.46 μm . The entry pressure varied from 0.03 to 0.67 MPa with an average of 0.21 MPa. The median saturation pressure ranged from 0.12 to 17.42 MPa with an average of 3.93 MPa. The maximum mercury saturation varied from 67.41 to 98.16% with an average of 83.42%. Based on the above data, it can be concluded that the E_{3h} reservoirs in Xihu Sag have various types of pore throat structure with wide distribution of pore-throat sizes.

By analyzing the HPMI data and the intrusion curves, four types of pore throat structures were identified in E_{3h} reservoirs (Figures 5 and 6) (Considering the effective range of MICP experiments and the distortion data at the nanoscale, Figure 6 only shows the pore size distribution larger than 10 nm). The Type I mercury intrusion curves showed a low entry pressure, which was less than 0.055 MPa. During the early stage of mercury injection, the amount of mercury intrusion grew slowly, and the mercury intrusion curves were kept almost horizontal for a long time. After the mercury saturation reached 42.82–47.73%, the amount of mercury intrusion increased rapidly, and mercury intrusion curves showed a larger slope. The maximum mercury saturations ranged from 88.85% to 98.16%. The pore throat distributions were unimodal, and their main peaks were distributed between 5 and 20 μm . The Type II mercury intrusion curves had a medium entry pressure ranging from 0.05 to 0.1 MPa. There was no obvious horizontal period in the mercury intrusion curves, and the whole curves were similar to a diagonal line, indicating the pore throat distribution was relatively average. The maximum mercury saturation of Type II was low, ranging from 67.41% to 70.7%. Their pore throat distributions were bimodal, indicating two kinds of pores with pore size ranging from 0.25–1.1 μm and 1.1–13 μm . The entry pressure of Type III mercury intrusion curves increased to 0.26 MPa. During the early stage of mercury injection, the mercury intrusion curves had an obvious horizontal period. After the mercury saturation reached 28.51–37.10%, the slope of the mercury intrusion curves increased, and the curves were located along a diagonal line. The maximum mercury saturation of Type III was relatively high with 88.85% and 98.16%. The peak of pore throat distribution was mainly concentrated between 0.35 and 2.8 μm . The Type IV mercury intrusion curves had the highest entry pressure which reached 0.67 MPa. There was a short horizontal period of the mercury intrusion curve during the early stage of mercury injection. After the mercury saturation reached 25.50%, the curve was nearly distributed along a diagonal line. The maximum mercury saturation reached 73.88%, and the pore throat distribution was unimodal with their main peak distribution between 0.26 and 1.1 μm . The reservoir quality represented by the four types of pore throat structure became gradually worsened from

Type I to Type IV. According to the reservoir quality index (RQI) in Table 2, Type I had the highest RQI values, with RQI values ranging from 1.25 to 2.08. The RQI values of Type II distributed between 1.05 and 0.95. The RQI values of Type III were lower than Type I and Type II, which ranged from 0.58 to 0.33. The RQI value of Type IV was the lowest with a value of 0.18.

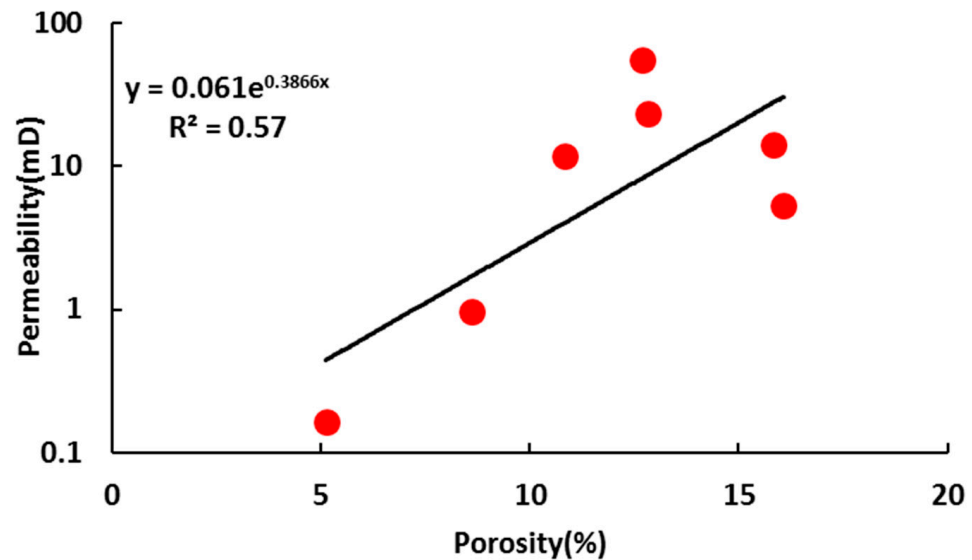


Figure 3. Relationship between porosity and permeability of the E₃h tight sandstone reservoirs in Xihu Sag.

Table 2. Microscopic pore structure parameters from HPMI analysis of E₃h tight sandstones in Xihu Sag.

Sample	Well	Depth (m)	RQI (μm)	Maximum Radius (μm)	Average Radius (μm)	Entry Pressure (MPa)	Median Pressure (MPa)	Relative Sorting Factor	Maximum Mercury Saturation (%)
1	Well A	3600.72	1.05	13.35	3.12	0.06	4.39	2.44	67.41
2	Well A	3961.62	0.18	1.10	0.22	0.67	17.42	15.91	73.88
3	Well A	3980.48	0.33	2.80	0.70	0.26	1.52	4.19	94.82
4	Well B	3742.45	1.35	13.36	4.54	0.06	0.27	1.01	88.85
5	Well B	3792.35	2.08	21.37	6.28	0.03	0.12	0.49	98.16
6	Well C	3126.45	0.95	6.68	1.47	0.11	2.59	4.05	70.70
7	Well C	3132.47	0.58	2.81	0.89	0.26	1.23	3.41	90.08

The HPMI results can clarify the relative contribution of different sizes of pore throat to permeability. It can be seen in Figure 7 that the contribution to permeability was concentrated in the large pore throat when the permeability contribution curve peak ranged from 0.63 to 10 μm. The higher the sample permeability, the better the reservoir quality, and the larger the pore throat size corresponding to the permeability contribution curve peak. The cumulative relative permeability curves of samples with different pore throat structures had similar trends. The cumulative relative permeability contribution increased rapidly and soon reached 90% in the early stage of mercury intrusion, with the formation of a steep curve. The trend of the curve then became flat and increased slowly. When the relative contribution of permeability reached 90%, the mercury saturation was only 16.41–49.14%, with an average of 30.93%. This indicated that small numbers of large pore throats dominated the relative permeability contribution and became the main factor influencing the permeability. The abundant small pore throats made a negligible contribution and controlled the storage capacity of the reservoir.

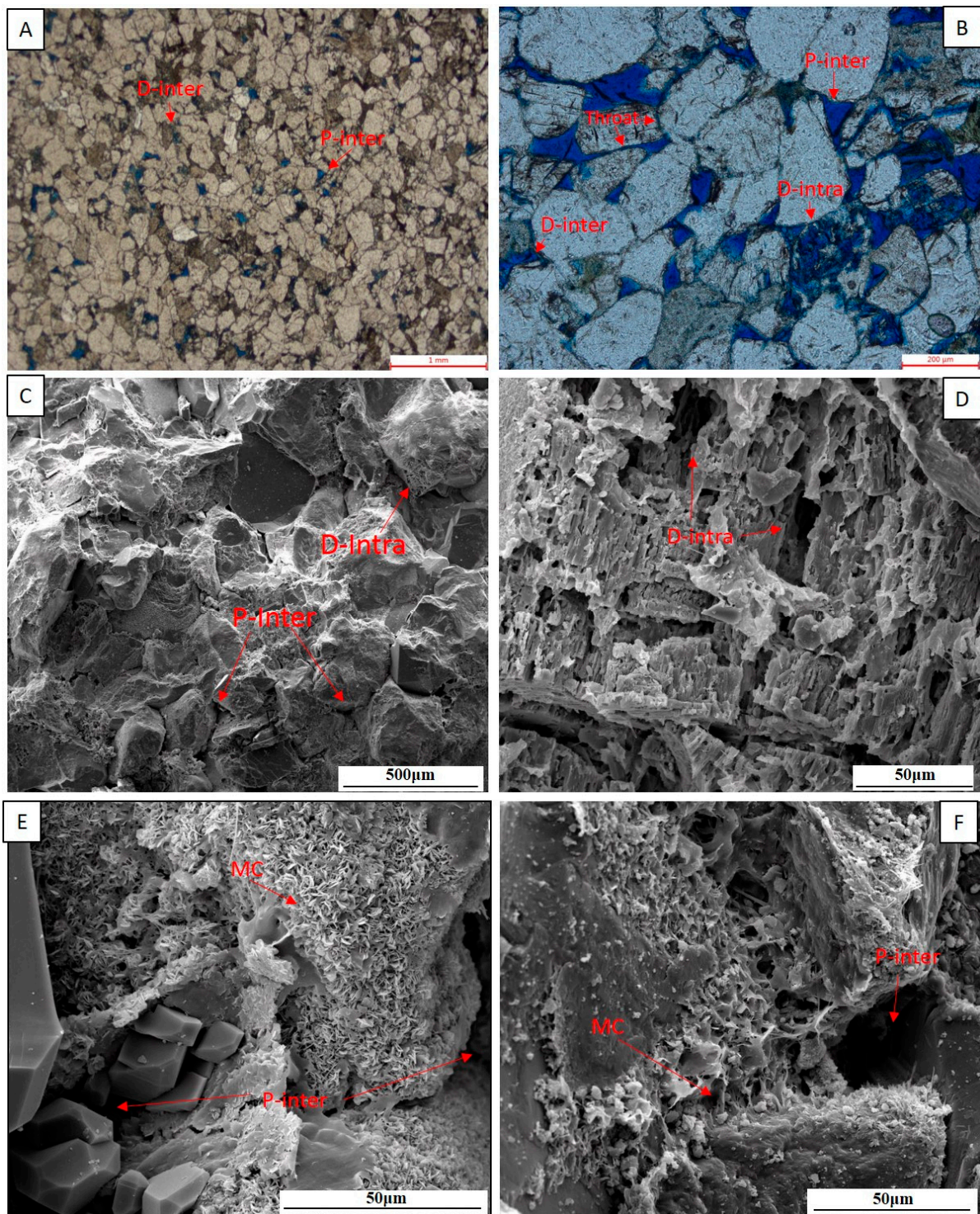


Figure 4. Pore type of the E_{3h} tight sandstones in Xihu Sag. Legend: P-Inter, primary intergranular pores; D-Inter, intergranular dissolution pores; D-Intra, intragranular dissolution pores; MC, micropores within clay aggregates. (A) Full view with primary pores predominating, Well A 3961.62 m; (B) Primary intergranular pores, intergranular dissolved pores, intragranular dissolved pores, Well B 3742.45 m; (C) Full view with lithology dense, Well A 3600.7 m; (D) Pores formed by dissolution of alkali feldspar, Well C 3126.5 m; (E) Autogenous quartz, chlorite, and illite distributed in primary intergranular pores, chlorite distributed on the grain surface, Well A 3980.6 m; (F) micropores formed in illite Well A 3961 m.

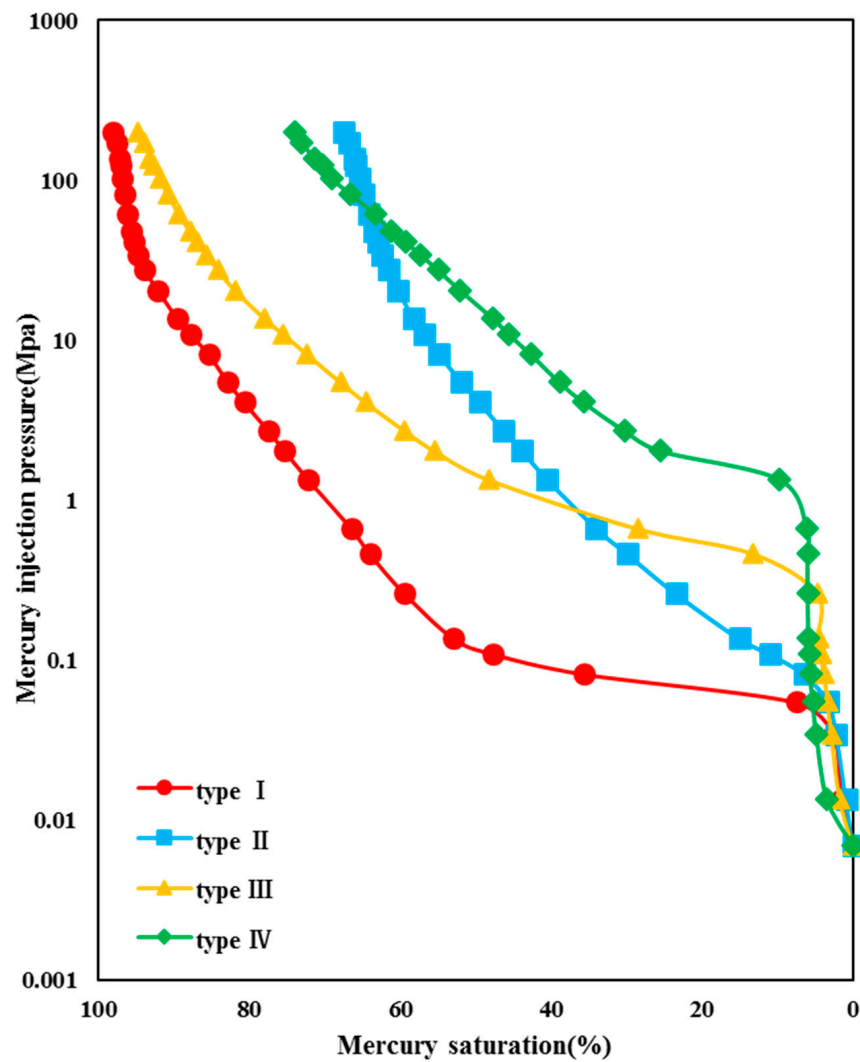


Figure 5. The mercury intrusion curves of the seven samples from HPMI analysis (Type I: Sample 5; Type II: Sample 1; Type III: Sample 3; Type IV: Sample 2).

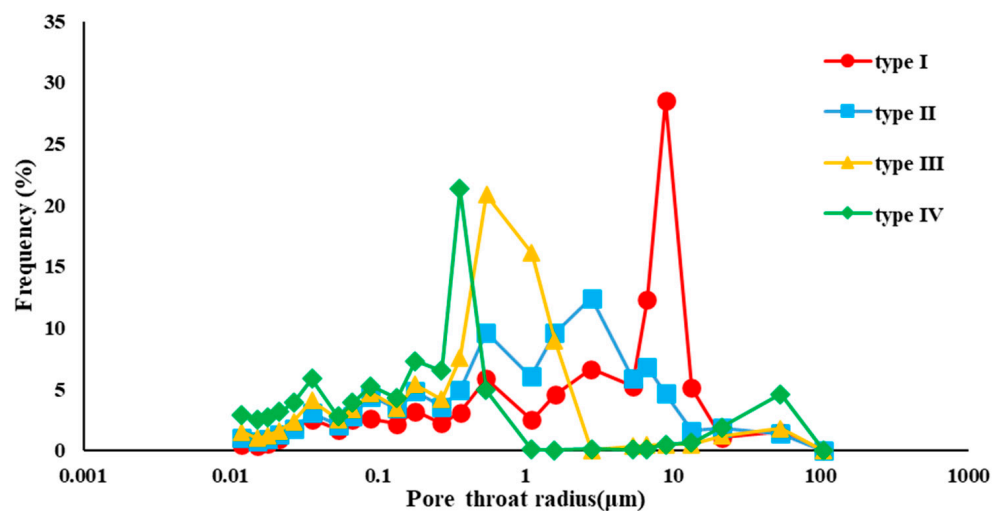


Figure 6. Pore throat distribution of the seven samples from HPMI analysis (Type I: Sample 5; Type II: Sample 1; Type III: Sample 3; Type IV: Sample 2).

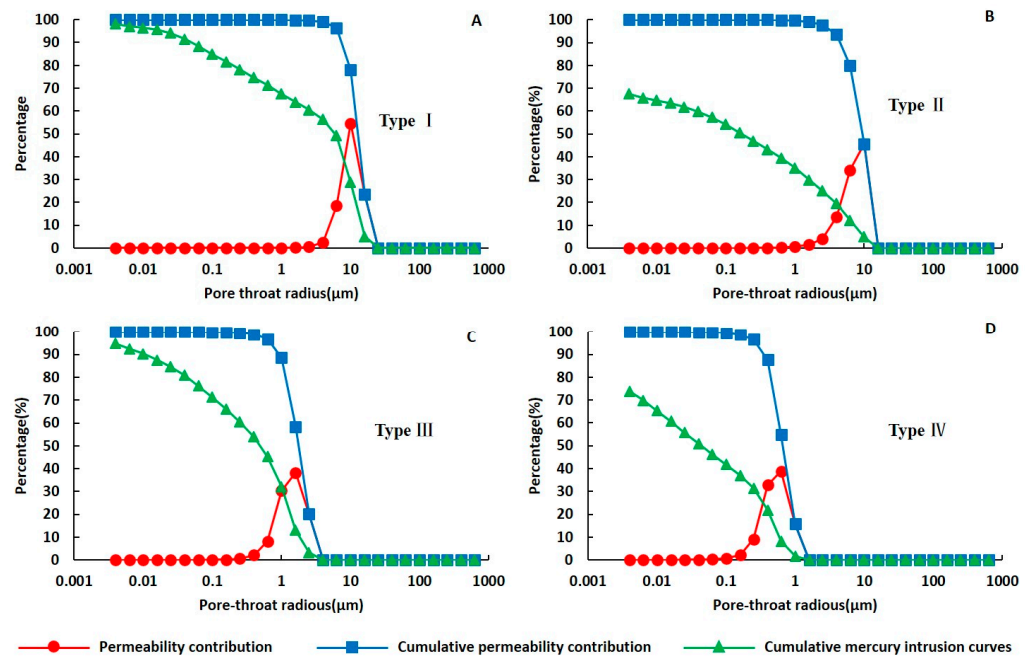


Figure 7. Permeability contributions of differently sized pore throats HPMI analysis (A) Sample 5; (B) Sample 1; (C) Sample 3; (D) Sample 2.

4.3. Pore Size Distributions from NMR

Table 3 showed the parameters obtained from NMR experiments, which included NMR porosity, $T_{2\text{peak}}$, $T_{2\text{gm}}$, $T_{2\text{cutoff}}$, S_{wi} , movable-fluid porosity, and bound-fluid porosity. The NMR porosity was in the range of 5.24–16.95% with an average of 11.81%. $T_{2\text{peak}}$, which was defined as the T_2 value that can show the highest frequency on the T_2 spectrum [41], had a wide range from 0.85 to 109.7 ms, and an average of 50.88 ms. $T_{2\text{gm}}$ varied from 2.38 to 33.39 ms with an average of 14.69 ms. The $T_{2\text{cutoff}}$, which distinguished the bound fluid residing in small pores and clay minerals from the movable fluid residing in large pores [42], ranged from 2.25 to 36.12 ms with an average of 10.54 ms. The S_{wi} ranged from 24.75 to 56.87% with an average of 41.28%. The movable porosity varied from 2.26 to 10.27% with an average of 7%. The bound-fluid porosity ranged from 2.83 to 8.47% with an average of 4.81%. The above data shed some light on the diversity and complexity of the pore structure of the samples in this study area. The T_2 spectrum ranged widely, from 0.1 ms to 1000 ms, mainly following the bimodal distribution (Figure 8). The left peaks were concentrated between 0.69 and 13.92 ms, and the right peaks ranged from 14.31 to 163.99 ms. The interval between the two peaks suggested the pore distribution was discontinuous, and the sorting of the pores was poor. Comparing the curve of water-saturated and after centrifugation with different centrifugal speeds, the short T_2 relaxation time of the left peak was attributed to small pores and poor connectivity. After centrifugation, the amplitude of the left peak was still high, which indicated the small pores mainly resided in irreducible water which was hard to remove by centrifugation. In contrast, the right peak corresponded to large pores with long T_2 relaxation time and good connectivity. The amplitude of the right peak decreased after centrifugation, which indicated the large pores mainly resided in moveable water, and most of the moveable water was centrifuged out. The four types of pore structure identified by HPMI also exhibited different characteristics in the NMR T_2 spectrum. The reservoir quality of Type I was the best among these four kinds of pores, and the right peak dominated the T_2 spectrum of Type I with long T_2 relaxation time (Figure 8A), showing relatively more abundance in large pores with good connectivity. During centrifugation, more than 50% of water was removed with 1000 r/min (Table 4). This means most of the full NMR signal was made of moveable water residing in large pores, and the S_{wi} was less than 30%. The reservoir quality of Type II and Type III

was medium, from which the T_2 spectrum was obviously bimodal, and the two peaks had a similar integral area (Figure 8B,C). During the centrifugation, the decline of amplitude for Type II was larger than for Type III. With the increasing centrifugal speed, the water saturation of Type II decreased from 76.21–63.01% to 47.64–30.18%, and Type III only decreased from 84.63–83.07% to 50.91–49.78% (Table 4). The irreducible water saturation of Type II and Type III was larger than Type I, and S_{wi} ranged from 30% to 50%. The reservoir quality of Type IV was the worst, and the left peak was the major peak in the T_2 spectrum (Figure 8D), corresponding to the small pores with poor connectivity. The small pores resided in irreducible water and limited the flow capacity of the reservoir. The greater the number of small pores, the more irreducible water, the stronger heterogeneity of the pore structure, and the worse the reservoir quality. Figure 8 and Table 4 showed that the decline of amplitude for Type IV was minimal. A large amount of irreducible water resided in the small pores, and a small amount of moveable water was removed by centrifugation. The irreducible water saturation of Type IV was the highest and reached 56.87%. The above results showed the large pores corresponding to long T_2 relaxation time were mainly full of moveable water, which was an important factor that influenced the flow capacity of the reservoir. The T_2 spectrum corresponding to the pore structure of different types was quite different, and the various type T_2 spectra reflected the diversity and heterogeneity of the pore structure of the samples in the study area.

Table 3. NMR parameters of E₃h tight sandstones in in Xihu Sag.

Sample	NMR Porosity (%)	T_{2peak} (ms)	T_{2gm} (ms)	$T_{2cutoff}$ (ms)	S_{wi} (%)	Movable-Fluid Porosity (%)	Bound-Fluid Porosity (%)
1	11.28	67.48	13.56	3.41	30.19	7.87	3.40
2	5.24	0.85	2.38	2.25	56.87	2.26	2.98
3	9.12	18.04	5.67	5.54	49.78	4.58	4.54
4	9.80	51.11	10.33	2.58	28.85	6.97	2.83
5	13.65	77.53	19.65	4.50	24.75	10.27	3.38
6	16.95	109.70	33.39	36.12	47.64	8.88	8.08
7	16.63	31.44	17.90	19.34	50.91	8.17	8.47

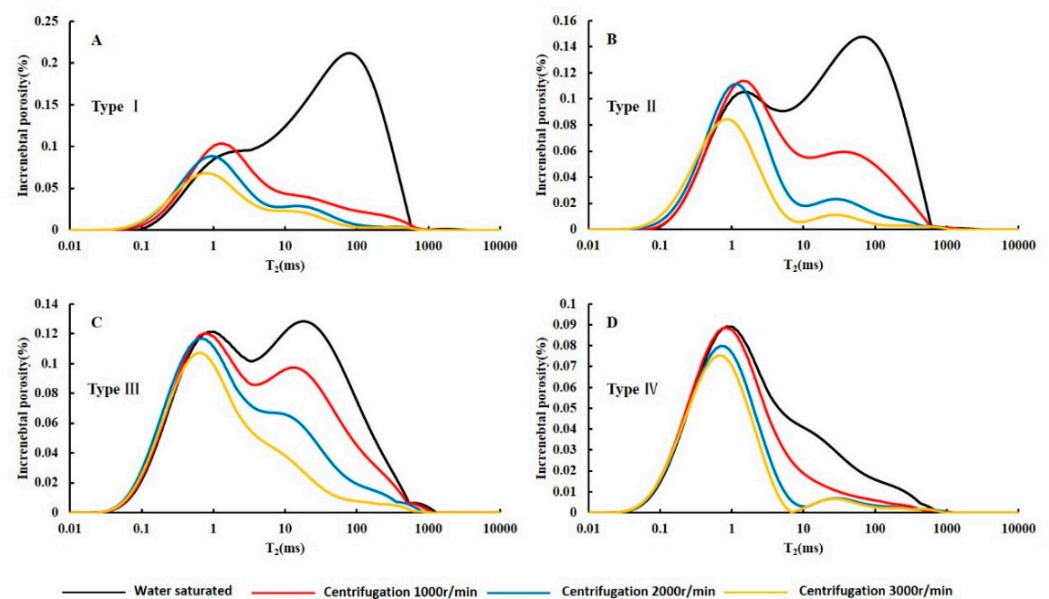


Figure 8. NMR T_2 incremental spectra for water saturated and centrifugation with different speeds. (A) Sample 5; (B) Sample 1; (C) Sample 3; (D) Sample 2.

Table 4. Water saturation of samples at different centrifugal speeds.

Sample	Water Saturation (%)		
	1000 r/min	2000 r/min	3000 r/min
1	63.01	42.51	30.19
2	80.19	62.47	56.87
3	83.07	65.88	49.78
4	51.97	38.42	28.85
5	41.54	31.17	24.75
6	76.21	59.93	47.64
7	84.63	64.10	50.91

4.4. Fractal Analysis from NMR with Centrifugation

According to Equation (14) and NMR data, the plot of $\log(f_r)$ versus $\log(T_2)$ can be used to show the fractal characteristics of pore structure for residual water at different centrifugal speeds (Figure 9). If there were no large pores with long relaxation times ($T_2 > 1000$ ms) existing in the samples, the slope of the curve would decrease and the curves would approach asymptotically the value $f_r = 1$. Therefore, the behavior of the curves for $f_r > 0.95$ was not important. [40]. The partial curves with small T_2 relaxation time showed similar problems. Since $r \gg r_{min}$ was the condition that was needed to enable the simplification of Equation (9) to get Equation (10), the value of T_2/T_{2min} must be larger than 9 [40]. Meanwhile, the pore throats and the clay mineral-dominated small pores generally corresponded to the short T_2 relaxation times, and this group of pore systems was not self-similar and therefore cannot be characterized by the fractal model [43]. As discussed above, the curves for $0.05 < f_r < 0.95$ were selected to determine the slope (Figure 9). The slope of $\log(f_r)$ versus $\log(T_2)$ were variations and showed segmentation in Figure 9, so it was not justified to assume a constant fractal dimension across the whole range of relaxation times [44]. The $T_{2cutoff}$, which separated the immovable water and movable water, can be used to segment the curves. In the calculation of fractal dimension for centrifugal NMR, the fractal dimensions calculated by the segment with T_2 were smaller than the $T_{2cutoff}$ which represented the fractal dimensions of small pores (D_s). In contrast, the fractal dimensions with T_2 were larger than the $T_{2cutoff}$ which represented the fractal dimensions of large pores (D_l) (Shao et al., 2017b). Table 5 shows the fractal analysis results from centrifugal NMR, and most of the correlation coefficients of linear fitting were larger than 0.95, which indicated the pore structure of residual water was fractal. Figures 10 and 11 show that with the increase in centrifugal speed, D_l became larger, and D_s obeyed a similar law. The variation of D_s in some samples was small or opposite, which may be due to the centrifugation having a slight influence on the water in small pores. Based on the fractal theory, the fractal dimensions of the pore structure were in the range of 2–3, and low fractal dimensions (closer to 2) indicated the simpleness of pore throat shapes and smoothness of pore throat surfaces. In contrast, large fractal dimensions (closer to 3) indicated the rough surfaces and complex structure [5]. The increase of the fractal dimensions reflected the discrete distribution of the pore throat and suggested the pore structure transformed from simple to complex, which consequently reduced the permeability and limited the flow capacity of the reservoir [45]. Based on the above analysis, with the increase of centrifugal speed, a large amount of water was removed, and the residual water was distributed in the pores with high fractal dimensions and complicated structure.

The $T_{2cutoff}$ value was used to divide the moveable fluid and the bound fluid in the NMR curve. However, in Figure 9, it is visible that some pores with T_2 values larger than the $T_{2cutoff}$ were still resided by fluid. Based on the difference values between the NMR curves of water-saturated and centrifuged samples, real pore size distribution and content of the dynamic variation in centrifugation can be reflected. According to Equation (14), the curves of the difference between T_2 spectrums in different centrifugation speeds could be used to calculate the fractal dimensions of the fluid variation (Figure 12), which includes the fractal dimensions of fluid variation between water saturated and 1000 r/min

(D₁), 1000 r/min and 2000 r/min (D₂), 2000 r/min and 3000 r/min (D₃). Table 6 shows the fractal analysis results of the fluid variation between different centrifugation speeds, and most of the samples showed that with the increase of centrifugal speed, the fractal dimensions of fluid variation became larger (Figure 13). It was indicated that in the process of centrifugation, the water residing in the pores with simple structures was removed preferentially, and with the increase of centrifugal speed, the water reserved in the pores with more complicated pore structures was removed gradually, which indicated the flow capability of reservoir was affected by the complexity of pore structure.

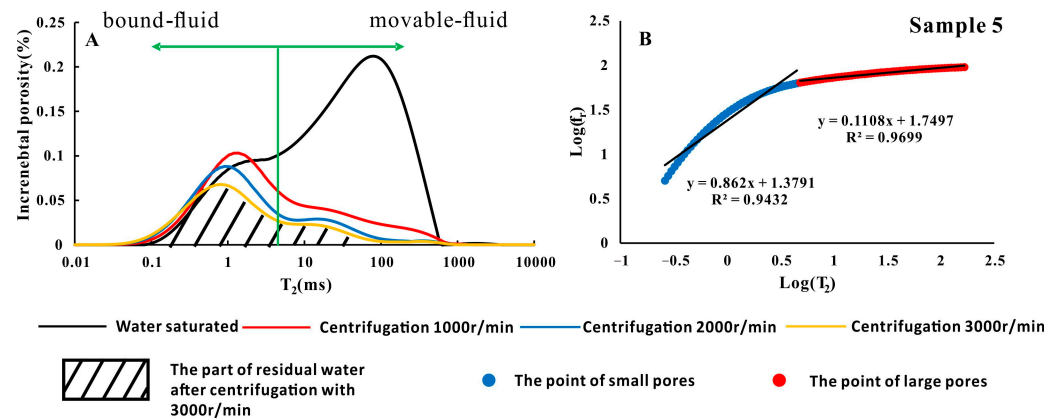


Figure 9. Plot of lg(fr) versus Lg(T₂) using NMR from Sample 5. (A) the residual water distribution; (B) fractal curve of the residual water.

Table 5. Fractal Dimensions of the residual water from NMR in different centrifugal speeds.

Sample	1000 r/min				2000 r/min				3000 r/min			
	D _s	R ²	D ₁	R ²	D _s	R ²	D ₁	R ²	D _s	R ²	D ₁	R ²
1	2.05	0.96	2.84	0.99	2.03	0.95	2.92	0.99	2.13	0.93	2.96	0.99
2	2.08	0.95	2.91	0.92	2.08	0.94	2.96	0.83	2.10	0.94	2.97	0.82
3	2.36	0.92	2.84	0.97	2.35	0.91	2.88	0.97	2.34	0.89	2.91	0.97
4	2.04	0.96	2.87	0.98	2.05	0.95	2.94	0.97	2.09	0.94	2.96	0.97
5	2.14	0.94	2.89	0.97	2.19	0.92	2.89	0.99	2.26	0.92	2.90	0.99
6	2.39	0.98	2.78	0.98	2.39	0.97	2.81	0.99	2.38	0.96	2.86	0.99
7	2.31	0.98	2.80	0.98	2.28	0.97	2.82	0.99	2.32	0.96	2.88	0.98

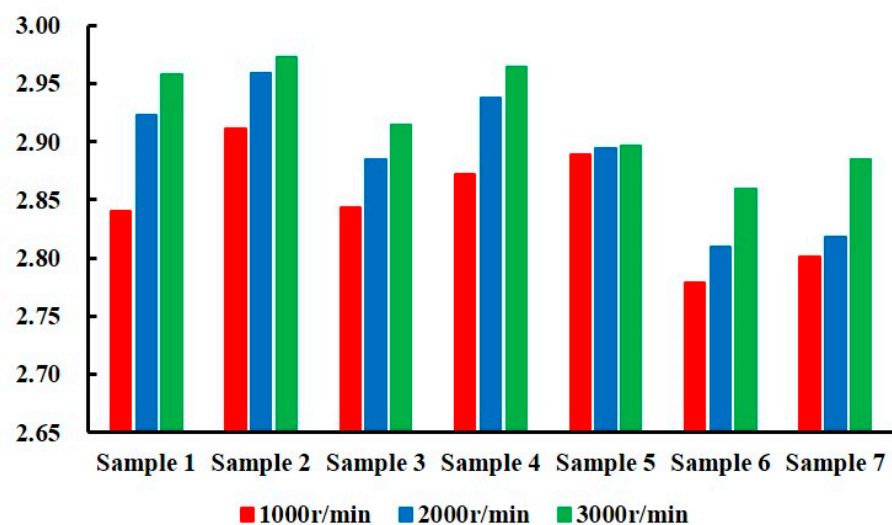


Figure 10. Trends of D₁ in different centrifugal speed.

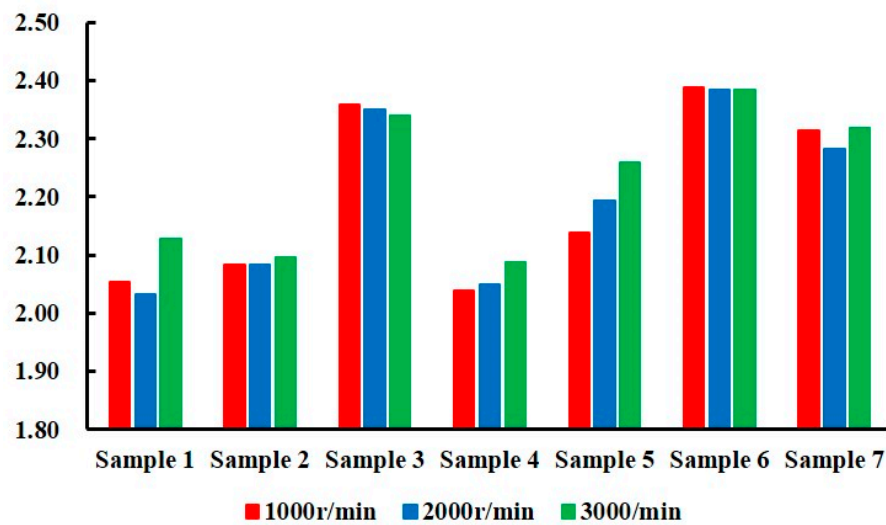


Figure 11. Trends of D_s in different centrifugal speeds.

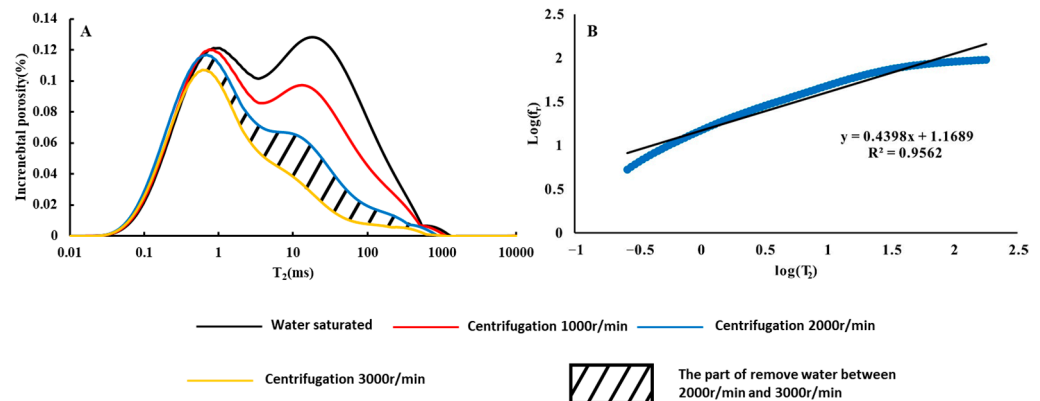


Figure 12. Plot of $\lg(f_r)$ versus $\lg(T_2)$ using NMR from Sample 3. (A) the removed water distribution; (B) fractal curve of the removed water.

Table 6. Fractal Dimensions of the residual water from NMR in different centrifugal speeds.

Sample	1000 r/min				2000 r/min				3000 r/min			
	D_s	R^2	D_1	R^2	D_s	R^2	D_1	R^2	D_s	R^2	D_1	R^2
1	2.05	0.96	2.84	0.99	2.03	0.95	2.92	0.99	2.13	0.93	2.96	0.99
2	2.08	0.95	2.91	0.92	2.08	0.94	2.96	0.83	2.10	0.94	2.97	0.82
3	2.36	0.92	2.84	0.97	2.35	0.91	2.88	0.97	2.34	0.89	2.91	0.97
4	2.04	0.96	2.87	0.98	2.05	0.95	2.94	0.97	2.09	0.94	2.96	0.97
5	2.14	0.94	2.89	0.97	2.19	0.92	2.89	0.99	2.26	0.92	2.90	0.99
6	2.39	0.98	2.78	0.98	2.39	0.97	2.81	0.99	2.38	0.96	2.86	0.99
7	2.31	0.98	2.80	0.98	2.28	0.97	2.82	0.99	2.32	0.96	2.88	0.98

4.5. Fractal Analysis from Water-Saturated NMR

According to the above method, the fractal characteristics can be calculated by the plot of $\log(V)$ versus $\log(T_2)$ (Figure 14). In the calculation of fractal dimension for water-saturated NMR, the fractal dimensions calculated by the segment with T_2 were larger than the $T_{2\text{cutoff}}$ that represented the fractal dimensions of movable-fluid pores (D_{mov}), and the fractal dimensions obtained from segments with T_2 were smaller than the $T_{2\text{cutoff}}$ that represented the fractal dimensions of bound-fluid pores (D_{bnd}) [45]. Table 7 shows the fractal analysis results from water-saturated NMR, and most of the correlation coefficients of linear fitting were larger than 0.95, which indicated the pore structure of reservoirs in

E_{3h} was fractal. The D_{bnd} ranged from 2.109 to 2.393 with an average of 2.253, whereas the D_{mov} ranged from 2.66 to 2.87 with an average of 2.751. According to Table 5, the D_{mov} was significantly larger than D_{bnd} , which indicated the movable-fluid pores were more complicated than bound-fluid pores.

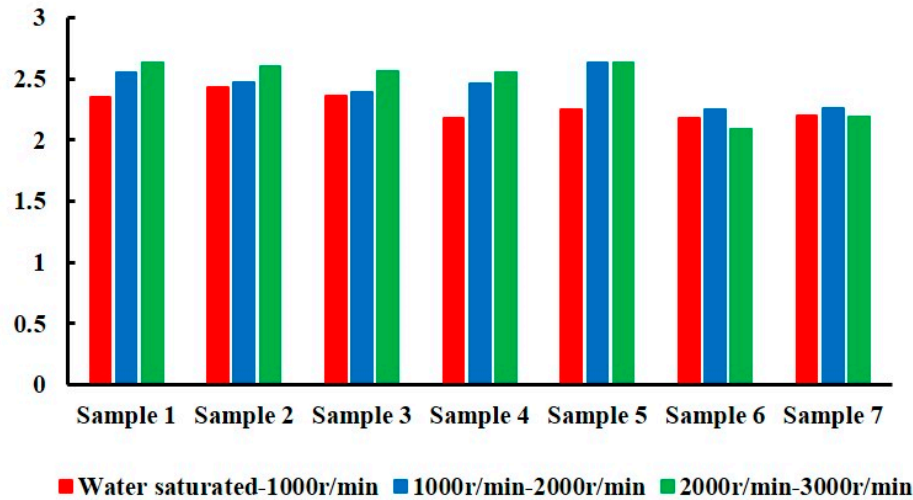


Figure 13. Trends of fractal dimension for fluid variation in different centrifugal speeds.

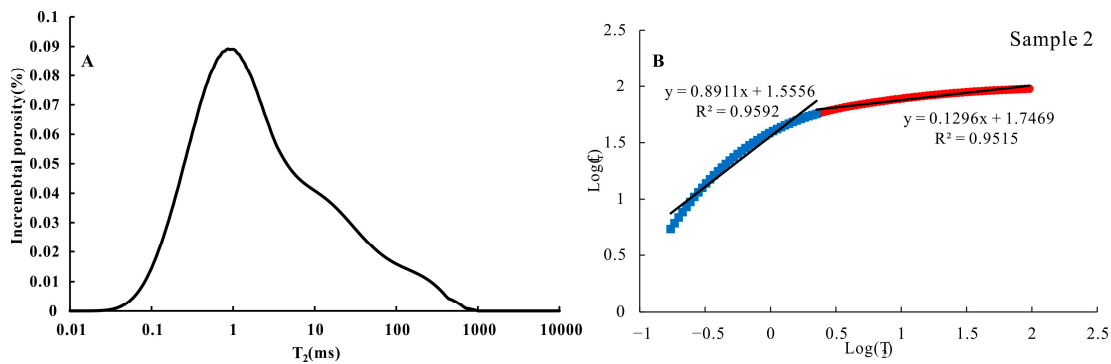


Figure 14. The plot of $\lg(f_r)$ versus $\lg(T_2)$ using NMR from Sample 2. (A) the saturated water distribution; (B) the fractal curve of saturated water.

Table 7. Fractal Dimensions of the samples from NMR with water saturated.

Sample	Bound-Fluid Pores		Movable-Fluid Pores	
	D_{bnd}	R^2	D_{mov}	R^2
1	2.168	0.968	2.725	0.993
2	2.109	0.959	2.870	0.952
3	2.359	0.930	2.803	0.974
4	2.158	0.976	2.697	0.997
5	2.272	0.975	2.660	0.992
6	2.393	0.980	2.741	0.980
7	2.315	0.984	2.762	0.978

Figure 15 shows the relationship between D_{mov} , D_{bnd} , permeability, and parameters of NMR. There was no obvious correlation between D_{mov} and D_{bnd} (Figure 15A), which indicated the movable-fluid pores and bound-fluid pores were not related to each other in the complex and heterogeneous pore structure. D_{mov} and D_{bnd} showed no obvious correlation with NMR porosity (Figure 15B,C), indicating the fractal characteristics of the reservoir showed little effect on storage space. D_{mov} showed a significantly negative correlation with

permeability (Figure 15D) and had a correlation coefficient of 0.972, whereas D_{bnd} showed no relationship with permeability (Figure 15E). D_{mov} had a negative correlation with the movable-fluid porosity with correlation coefficients of 0.804 (Figure 15F), whereas D_{bnd} showed a positive correlation with the bound-fluid porosity and the correlation coefficient was 0.645 (Figure 15G). These results suggested that the fractal dimensions influenced the flow capability of reservoirs significantly, and with the increase of D_{mov} , the pore structure became more complicated and the flow capacity of the reservoir became worse. In addition, when the D_{mov} increases, the permeability reduces, the movable-fluid pores decrease and the quality of the reservoir is poor. The movable-fluid pores controlled the flow capacity of tight sandstone reservoirs. D_{mov} also showed good correlation with the $T_{2\text{peak}}$ and S_{wi} (Figure 15H,I), which proved D_{mov} was a good indicator to characterize reservoir quality of $E_3\text{h}$ tight sandstone reservoirs.

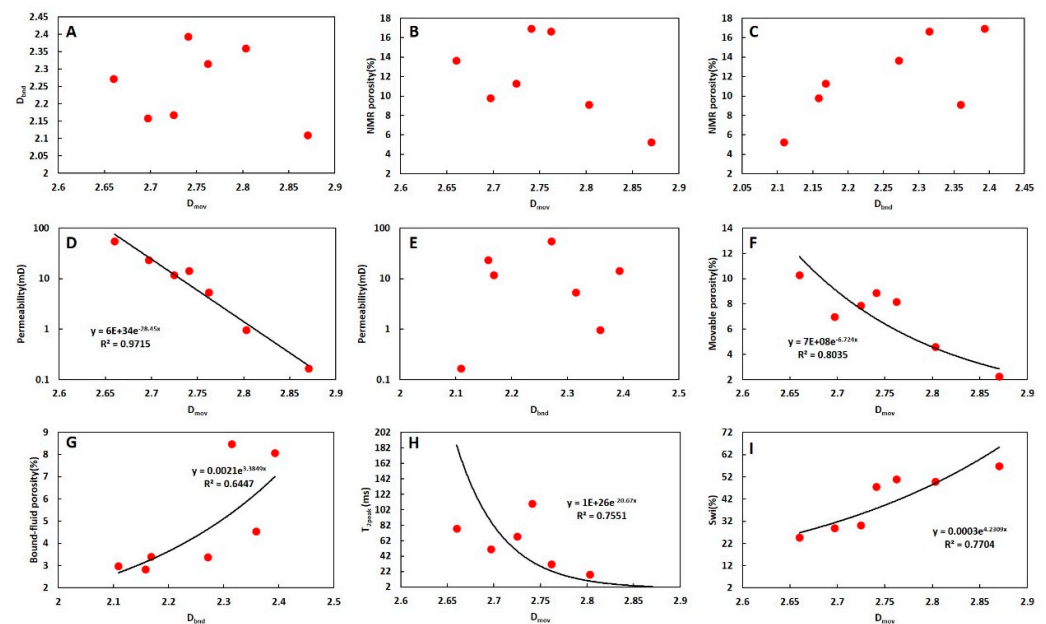


Figure 15. Plot showing the relationships between (A) D_{mov} and D_{bnd} ; (B) D_{mov} and NMR porosity; (C) D_{bnd} and NMR porosity; (D) D_{mov} and Permeability; (E) D_{bnd} and Permeability; (F) D_{mov} and Movable-fluid porosity; (G) D_{bnd} and Bound-fluid porosity; (H) D_{mov} and $T_{2\text{peak}}$; (I) D_{mov} and S_{wi} .

4.6. Fractal Analysis from HPMT

According to Equation (12), Figure 16 shows the fractal characteristics of pore structure derived from HPMT. The curves of $\log(1 - S_{H_2})$ against $\log(Pc)$ were not a straight line, and they can be divided into three straight lines based on the variations of the slope. Figure 16 shows an example of such a plot for Sample 3, and the coefficients of linear regressions were larger than 0.95, which indicated the pore structure of Sample 3 had fractal behavior. The three segments represented the pores with different pore-throat radii: macropores (100–1 μm), mesopores (1–0.1 μm), and micropores (<0.1 μm). Table 8 shows the fractal analysis results of all samples, and most of the correlation coefficients of linear fitting were larger than 0.95, which proved the tight sandstone reservoirs in $E_3\text{h}$ were generally fractal. The fractal dimensions of macropores (D_{mac}) ranged from 2.967 to 2.988 and had an average of 2.981. The fractal dimensions of mesopores (D_{mes}) ranged from 2.614 to 2.844 with an average of 2.741. The fractal dimensions of micropores (D_{mic}) varied from 2.404 to 2.910 and had an average of 2.693. The data showed D_{mac} value was close to 3, which was larger than D_{mes} and D_{mic} . Therefore, the pore structure of macropores was more heterogeneous and complicated than mesopores and micropores in the $E_3\text{h}$ reservoir. This was consistent with the conclusion obtained from fractal analysis of water-saturated NMR and previous studies [19].

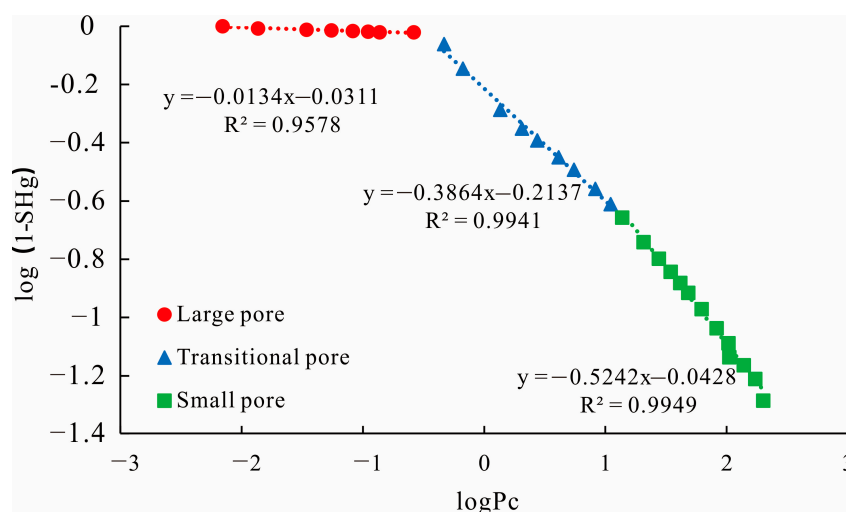


Figure 16. Plot of lg(1-SHg) versus lgPc using HPMI from Sample 3.

Table 8. Fractal Dimensions of the samples from IPMI.

Sample	Small Pores		Transitional Pores		Large Pores	
	D _s	R ²	D _t	R ²	D _l	R ²
1	2.910	0.984	2.844	0.999	2.984	0.987
2	2.717	0.999	2.815	0.998	2.987	0.784
3	2.476	0.995	2.614	0.994	2.987	0.959
4	2.753	0.992	2.803	0.990	2.969	0.831
5	2.404	0.983	2.720	0.987	2.967	0.787
6	2.888	0.942	2.774	0.992	2.985	0.975
7	2.706	0.997	2.620	0.996	2.988	0.993

Figure 17 shows the relationship between D_{mac} , D_{mes} , D_{mic} , and parameters from physical properties and HPMI. There were no meaningful correlations between D_{mac} , D_{mes} , and D_{mic} (Figure 17A–C), which indicated the complexity and heterogeneity of macropores, mesopores, and micropores that were not related to each other. Samples with greater complexity of macropores structures will not necessarily show very complex micropores structures, and they are independent of each other (Liu et al., 2018). D_{mac} , D_{mes} , and D_{mic} showed no discernible correlations with the porosity (Figure 17D–F), indicating that the storage space of the reservoir was not related to the complexity of the pore structure. D_{mes} and D_{mic} showed no relationship with the permeability (Figure 17H,I), while D_{mac} showed a negative correlation with the permeability (Figure 17G), and the correlation coefficient was 0.765. D_{mac} also showed a negative correlation with the average pore-throat radius with correlation coefficients of 0.870 (Figure 17J) and showed a positive correlation with median pressure with correlation coefficients of 0.675 (Figure 17K). These results indicated that with the increase of D_{mac} , the surface of the large pores became rougher, the average radius became smaller, the median pressure became high, and the pore structure became more complicated, resulting in the poor flow capacity of the reservoirs. D_{mic} showed a negative correlation with the maximum mercury saturation (Figure 17L) with a correlation coefficient of 0.763. The increase of D_{mic} reflected the pore structure of small pores became more complex and made it more difficult for mercury to be injected into micropores, which resulted in the increase of unsaturated pore volume and the decrease of the maximum mercury saturation. Overall, D_{mac} in E₃h tight sandstone was larger than D_{mes} and D_{mic} , which suggested the pore structure of the macropores was more complicated. Meanwhile, the macropores dominated the flow capacity of tight sandstone reservoirs, and the D_{mac} was an effective indicator of reservoir quality for E₃h tight sandstone reservoirs.

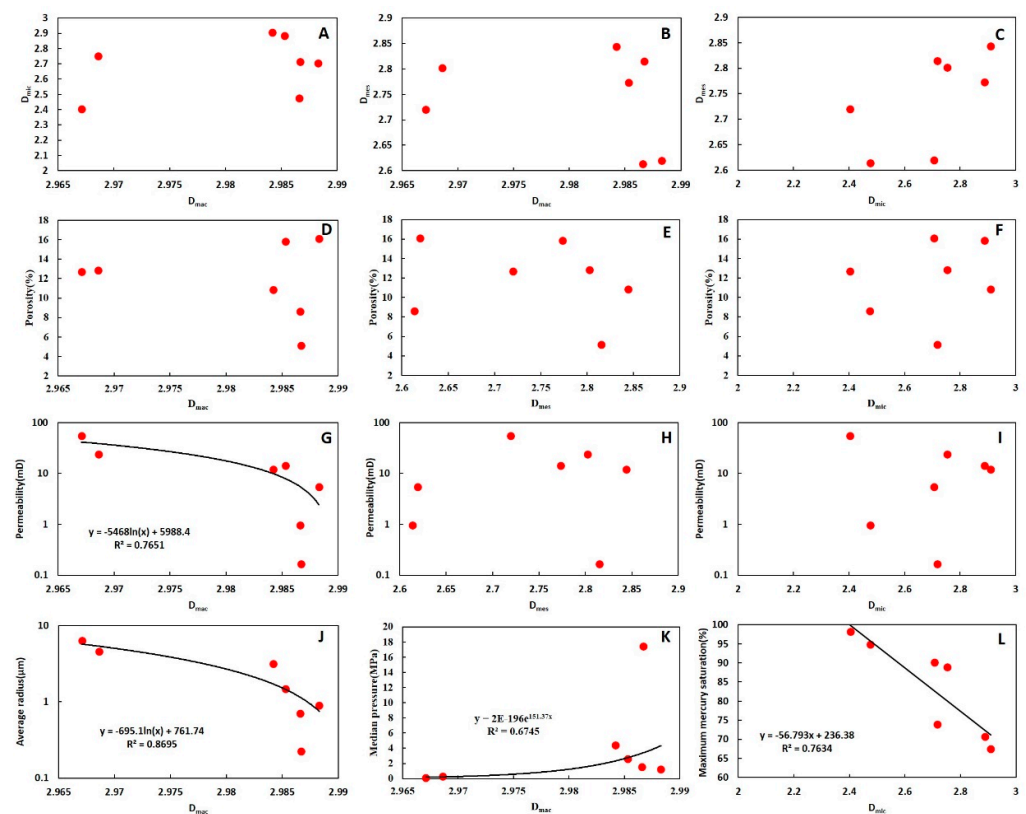


Figure 17. Plot showing the relationships between (A) D_{mac} and D_{mic} ; (B) D_{mac} and D_{mes} ; (C) D_{mes} and D_{mic} ; (D) Porosity and D_{mac} ; (E) Porosity and D_{mes} ; (F) Porosity and D_{mic} ; (G) Permeability and D_{mac} ; (H) Permeability and D_{mes} ; (I) Permeability and D_{mic} ; (J) Average radius and D_{mac} ; (K) Median pressure and D_{mac} ; (L) Maximum mercury saturation and D_{mic} .

4.7. Comparison of Fractal Analysis from HPMI and NMR

When comparing the fractal dimensions in Tables 7 and 8, it can be found that the fractal dimensions from HPMI and NMR show similar features. Figure 18 shows that D_{mic} to D_{mac} and D_{bnd} to D_{mov} both showed increasing trends, which indicated the fractal dimensions increased with increasing the pore throat radius and T_2 . In other words, the fractal dimensions of large pores were larger than those of small pores, and the pore structure of large pores was more complicated than those of small pores. Based on the above results, D_{mac} and D_{mov} both showed a high correlation with parameters of reservoir quality (permeability, average pore-throat radius, movable porosity S_{wi} , and T_{2peak}) and can reflect the quality of the reservoir effectively. Comparing the fractal dimensions of HPMI and NMR (Figure 19), there showed no obvious correlations among the fractal dimensions (Figure 19B–F) except D_{mac} and D_{mov} (Figure 19A). D_{mac} showed a positive correlation with D_{mov} , with a correlation coefficient of 0.57. As D_{mac} increased, D_{mov} also increased, which indicated the variation trend for fractal dimensions of the large pores from HPMI and NMR were consistent. The poor correlations among most of the fractal dimensions from HPMI and NMR may be caused by two reasons. The first reason is due to the different experimental designs of HPMI and NMR. In HPMI experiments, mercury was injected into samples by high pressure, and the mercury saturation was measured at different pressures. The distribution of the throat and its connected pores can then be obtained [5,46]. The NMR experiments collected the signal of echo attenuation from samples with saturated water, and the T_2 spectrum was calculated by mathematical inversion, which can be further transformed into the pore size distribution [24,33]. The HPMI experiments were focused on the pore throat size, whereas NMR experiments were more sensitive to pore body sizes. Therefore, these differences in the experiment method between HPMI and NMR resulted in the different and unmatchable fractal dimensions obtained by HPMI and NMR with

poor correlations between them. The second reason is the different partitioning methods for measuring fractal dimensions from HPMI and NMR. The fractal dimensions of samples were difficult to characterize by a constant value, therefore the pore size distribution of the samples was divided to obtain the fractal dimensions of each segment. In the fractal analysis of HPMI, the fractal dimensions were divided into three segments with different pore-throat radii: macropores (1–100 μm), mesopores (1–0.1 μm), and micropores (<0.1 μm). In NMR experiments, the curves of $\log(V)$ versus $\log(T_2)$ were divided into bound-fluid pores and movable-fluid pores by $T_{2\text{cutoff}}$. The different partitioning methods made the pore size distribution of fractal dimensions different, also resulting in the poor correlations of the fractal dimensions from HPMI and NMR.

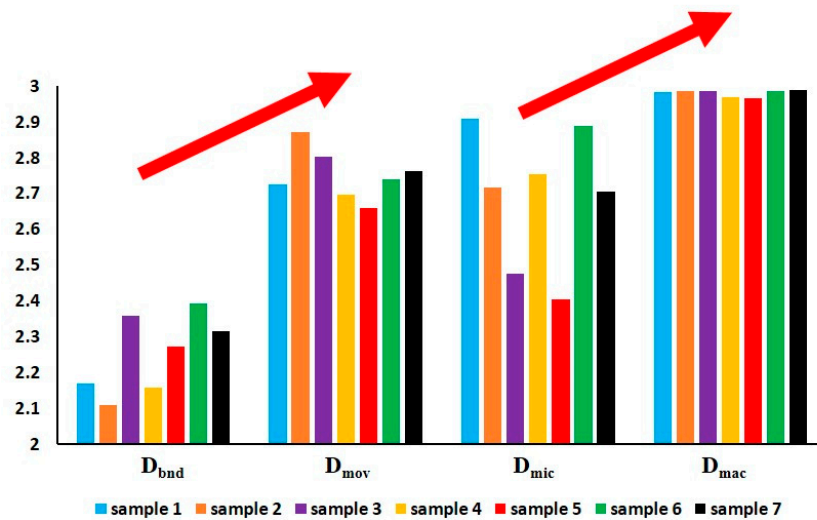


Figure 18. Trends of fractal dimensions from NMR and HPMI.

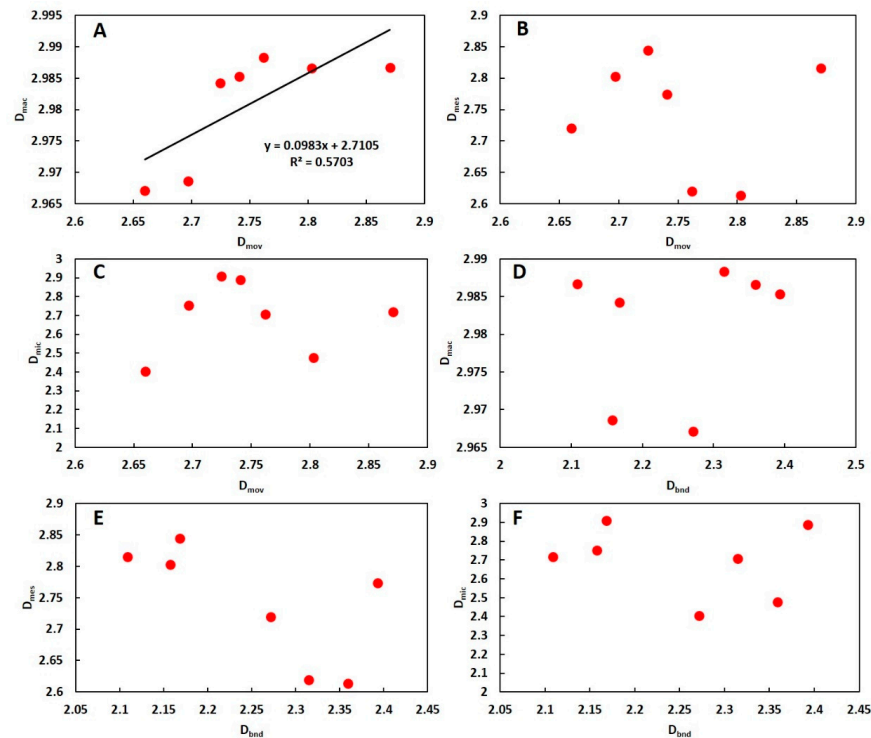


Figure 19. Plot showing the relationships between (A) D_{mov} and D_{mac} ; (B) D_{mov} and D_{mes} ; (C) D_{mov} and D_{mic} ; (D) D_{bnd} and D_{mac} ; (E) D_{bnd} and D_{mes} ; (F) D_{bnd} and D_{mic} .

5. Conclusions

The E₃h formation in Xihu Sag, East China Sea Basin, was dominated by tight sandstone reservoirs. There were four types of pores observed in the E₃h tight sandstone reservoirs: primary intergranular pores, intergranular dissolution pores, intragranular dissolution pores, and micropores within clay aggregates, and the morphology and size of different types of pores varied widely. By using HPMI and NMR, the four types of pore throat distributions were identified, which indicated the formation of complicated pore structures in the studied reservoir. The flow capability of E₃h reservoirs was controlled by large pores, while the small pores controlled the storage capability.

The centrifugal NMR data were used to analyze the dynamic variation of fractal dimensions of the pores with fluid resided during centrifugation. It was found that when the centrifugal speed increases, the water residing in the pores with simple structures is removed preferentially, and the pores with residual water are always more complicated than the pores with removed water. It indicated that the flow capability of the reservoir was affected by the complexity of the pore structure, and the flow capability of the reservoirs with low fractal dimensions and simple pore structure was stronger.

Based on the water-saturated NMR and HPMI data of E₃h reservoirs, fractal dimensions were calculated and compared. It is found that variation trends were consistent, which indicated that the fractal dimensions became larger with the increasing pore throat radius. The large pores dominated the flow capacity of E₃h reservoirs. D_{mac} and D_{mov} showed good correlations with permeability, average pore-throat radius, movable porosity, S_{wi} , and T_{2peak} , which can be used to reflect the reservoir quality effectively. The poor correlations between the fractal dimensions from HPMI and NMR were due to the difference in experimental methods and partitioning methods between HPMI and NMR.

Author Contributions: Conceptualization, J.D. and Z.H.; methodology, J.D.; software, J.D.; validation, J.C., J.Z., Y.P. and T.Q.; formal analysis, T.L.; investigation, J.C.; resources, Z.H.; data curation, J.D. and J.C.; writing—original draft preparation, J.D.; writing—review and editing, Z.H.; visualization, J.Z.; project administration, Z.H.; funding acquisition, Z.H. All authors have read and agreed to the published version of the manuscript.

Funding: This research was funded by National Science and Technology Major Project (No. 2016ZX05027-002-001).

Institutional Review Board Statement: This study does not involve humans or animals and not applicable for the ethical review and approval.

Informed Consent Statement: Not applicable.

Data Availability Statement: The data that support the findings of this study are available on request from the corresponding author, upon reasonable request.

Acknowledgments: Thanks to the funds provided by the National Major Science and Technology Project of China (No. 2016ZX05027-002-001), guidance provided by China University of Petroleum (Beijing), and experiment and testing support sponsored by the State Key Laboratory of Petroleum Resources and Prospecting, Beijing, and some of the data provided by Research Center and Exploration Department of China National Offshore Oil Corporation (CNOOC). We thank Feixue Liu for her valuable suggestions. We are also grateful to anonymous reviewers for their selfless contribution to the better publication and refinement of this paper.

Conflicts of Interest: The authors declare no conflict of interest.

References

1. Kang, Y.; Luo, P. Current status and prospect of key techniques for exploration and production of tight sandstone gas reservoirs in China. *Pet. Explor. Dev.* **2007**, *34*, 239–245.
2. Dai, J.; Ni, Y.; Wu, X. Tight gas in China and its significance in exploration and exploitation. *Pet. Explor. Dev.* **2012**, *39*, 257–264. [[CrossRef](#)]
3. Zou, C.; Zhu, R.; Liu, K.; Su, L.; Bai, B.; Zhang, X.; Yuan, X.; Wang, J. Tight gas sandstone reservoirs in China: Characteristics and recognition criteria. *J. Pet. Sci. Eng.* **2012**, *88*, 82–91. [[CrossRef](#)]

4. Gao, H.; Li, H.A. Pore structure characterization, permeability evaluation and enhanced gas recovery techniques of tight gas sandstones. *J. Nat. Gas Sci. Eng.* **2016**, *28*, 536–547. [[CrossRef](#)]
5. Li, P.; Zheng, M.; Bi, H.; Wu, S.; Wang, X. Pore throat structure and fractal characteristics of tight oil sandstone: A case study in the Ordos Basin, China. *J. Pet. Sci. Eng.* **2017**, *149*, 665–674. [[CrossRef](#)]
6. Anovitz, L.M.; Cole, D.R. Characterization and analysis of porosity and pore structures. *Rev. Mineral. Geochem.* **2015**, *80*, 61–164. [[CrossRef](#)]
7. Lai, J.; Wang, G.; Wang, Z.; Chen, J.; Pang, X.; Wang, S.; Zhou, Z.; He, Z.; Qin, Z.; Fan, X. A review on pore structure characterization in tight sandstones. *Earth-Sci. Rev.* **2018**, *177*, 436–457. [[CrossRef](#)]
8. Schmitt, M.; Fernandes, C.P.; Wolf, F.G.; Neto, J.A.B.C.; Rahner, C.P.; Santos, V.S.S.D. Characterization of Brazilian tight gas sandstones relating permeability and Angstrom-to micron-scale pore structures. *J. Nat. Gas Sci. Eng.* **2015**, *27*, 785–807. [[CrossRef](#)]
9. Fu, H.; Wang, X.; Zhang, L.; Gao, R.; Li, Z.; Xu, T.; Zhu, X.; Xu, W.; Li, Q. Investigation of the factors that control the development of pore structure in lacustrine shale: A case study of block X in the Ordos basin, China. *J. Nat. Gas Sci. Eng.* **2015**, *26*, 1422–1432. [[CrossRef](#)]
10. Taylor, T.R.; Giles, M.R.; Hathon, L.A.; Diggs, T.N.; Braunsdorf, N.R.; Birbiglia, G.V.; Espejo, I.S. Sandstone diagenesis and reservoir quality prediction: Models, myths, and reality. *AAPG Bull.* **2010**, *94*, 1093–1132. [[CrossRef](#)]
11. Golab, A.N.; Knackstedt, M.A.; Averdunk, H.; Senden, T. 3D porosity and mineralogy characterization in tight gas sandstones. *Lead. Edge* **2010**, *29*, 1476–1483. [[CrossRef](#)]
12. Bera, B.; Mitra, S.K.; Vick, D. Understanding the micro structure of Berea Sandstone by the simultaneous use of micro-computed tomography (micro-CT) and focused ion beam-scanning electron microscopy (FIB-SEM). *Micron* **2011**, *42*, 412–418. [[CrossRef](#)] [[PubMed](#)]
13. Comisky, J.T.; Newsham, K.E.; Rushing, J.A.; Blasingame, T.A. A comparative study of capillary-pressure-based empirical models for estimating absolute permeability in tight gas sands. In Proceedings of the SPE Annual Technical Conference and Exhibition, Anaheim, CA, USA, 11–14 November 2007; p. 110050.
14. Liu, K.; Ostadhassan, M.; Kong, L. Fractal and multifractal characteristics of pore throats in the Bakken Shale. *Transp. Porous Media* **2019**, *126*, 579–598. [[CrossRef](#)]
15. Zhao, P.; Wang, Z.; Sun, Z.; Cai, J.; Wang, L. Investigation on the pore structure and multifractal characteristics of tight oil reservoirs using NMR measurements: Permian Lucaogou Formation in Jimusaer Sag, Junggar Basin. *Mar. Pet. Geol.* **2017**, *86*, 1067–1081. [[CrossRef](#)]
16. Labani, M.M.; Rezaee, R.; Saedi, A.; Hinai, A.A. Evaluation of pore size spectrum of gas shale reservoirs using low pressure nitrogen adsorption, gas expansion and mercury porosimetry: A case study from the Perth and Canning basins, western Australia. *J. Pet. Sci. Eng.* **2013**, *112*, 7–16. [[CrossRef](#)]
17. Cao, Z.; Liu, G.; Zhan, H.; Li, C.; You, Y.; Yang, C.; Jiang, H. Pore structure characterization of Chang-7 tight sandstone using MICP combined with N₂GA techniques and its geological control factors. *Sci. Rep.* **2016**, *6*, 36919. [[CrossRef](#)] [[PubMed](#)]
18. Maniscalco, R.; Fazio, E.; Punturo, R.; Cirrincione, R.; Di Stefano, A.; Distefano, S.; Forzese, M.; Lanzafame, G.; Leonardi, G.S.; Montalbano, S.; et al. The porosity in heterogeneous carbonate reservoir rocks: Tectonic versus diagenetic imprint—A multi-scale study from the hyblean plateau (SE Sicily, Italy). *Geosciences* **2022**, *12*, 149. [[CrossRef](#)]
19. Shao, X.; Pang, X.; Jiang, F.; Li, L.; Huyan, Y.; Zheng, D. Reservoir characterization of tight sandstones using nuclear magnetic resonance and incremental pressure mercury injection experiments: Implication for tight sand gas reservoir quality. *Energy Fuels* **2017**, *31*, 10420–10431. [[CrossRef](#)]
20. Broseta, D.; Barré, L.; Vizika, O.; Shahidzadeh, N.; Guilbaud, J.-P.; Lyonnard, S. Capillary condensation in a fractal porous medium. *Phys. Rev. Lett.* **2001**, *86*, 5313–5316. [[CrossRef](#)]
21. Sakhaee-Pour, A.; Li, W. Fractal dimensions of shale. *J. Nat. Gas Sci. Eng.* **2016**, *30*, 578–582. [[CrossRef](#)]
22. Katz, A.J.; Thompson, A.H. Fractal sandstone pores: Implications for conductivity and pore formation. *Phys. Rev. Lett.* **1985**, *54*, 1325–1328. [[CrossRef](#)] [[PubMed](#)]
23. Guo, X.; Huang, Z.; Zhao, L.; Han, W.; Ding, C.; Sun, X.; Yan, R.; Zhang, T.; Yang, X.; Wang, R. Pore structure and multi-fractal analysis of tight sandstone using MIP, NMR and NMRC methods: A case study from the Kuqa depression, China. *J. Pet. Sci. Eng.* **2019**, *178*, 544–558. [[CrossRef](#)]
24. Lai, J.; Wang, G.; Fan, Z.; Chen, J.; Wang, S.; Zhou, Z.; Fan, X. Insight into the pore structure of tight sandstones using NMR and HPMI measurements. *Energy Fuel.* **2016**, *30*, 10200–10214. [[CrossRef](#)]
25. Su, A.; Chen, H.; Chen, X.; He, C.; Liu, H.; Li, Q.; Wang, C. The characteristics of low permeability reservoirs, gas origin, generation and charge in the central and western Xihu Depression, east China sea basin. *J. Nat. Gas Sci. Eng.* **2018**, *53*, 94–109. [[CrossRef](#)]
26. Xiao, D.; Lu, Z.; Jiang, S.; Lu, S. Comparison and integration of experimental methods to characterize the full-range pore features of tight gas sandstone—A case study in Songliao basin of China. *J. Nat. Gas Sci. Eng.* **2016**, *34*, 1412–1421. [[CrossRef](#)]
27. Jiang, S.; Li, S.; Chen, X.; Zhang, H.; Wang, G. Simulation of oil–gas migration and accumulation in the east China sea continental shelf basin: A case study from the Xihu depression. *Geol. J.* **2016**, *51*, 229–243. [[CrossRef](#)]
28. Zhao, Z.; Dong, C.; Zhang, X.; Lin, C.; Huang, X.; Duan, D.; Lin, J.; Zeng, F.; Li, D. Reservoir controlling factors of the Paleogene Oligocene Huagang formation in the north central part of the Xihu Depression, East China Sea Basin, China. *J. Pet. Sci. Eng.* **2019**, *175*, 159–172.

29. Hao, L.; Wang, Q.; Guo, R.; Tuo, C.; Ma, D.; Mou, W.; Tian, B. Diagenetic fluids evolution of Oligocene Huagang Formation sandstone reservoir in the south of Xihu Sag, the East China Sea Shelf Basin: Constraints from petrology, mineralogy, and isotope geochemistry. *Acta Oceanol. Sin.* **2018**, *37*, 25–34. [[CrossRef](#)]
30. Zhang, J.; Yu, Y.; Zhang, T.; Zhang, S.; Tang, X. A discussion on the exploration potential of deep basin gas in Xihu sag, East China Sea. *China Offshore Oil Gas* **2013**, *25*, 24–29.
31. Nooruddin, H.A.; Hossain, M.E.; Hasan, A.; Okasha, T. Comparison of permeability models using mercury injection capillary pressure data on carbonate rock samples. *J. Pet. Sci. Eng.* **2014**, *121*, 9–22. [[CrossRef](#)]
32. Washburn, E.W. Note on a method of determining the distribution of pore sizes in a porous material. *Proc. Natl. Acad. Sci. USA* **1921**, *7*, 115–116. [[CrossRef](#)]
33. Daigle, H.; Thomas, B.; Rowe, H.; Nieto, M. Nuclear magnetic resonance characterization of shallow marine sediments from the Nankai Trough, Integrated Ocean Drilling Program Expedition 333. *J. Geophys. Res. Solid Earth* **2014**, *119*, 2631–2650. [[CrossRef](#)]
34. Müller-Huber, E.; Schön, J.; Börner, F. Pore space characterization in carbonate rocks—Approach to combine nuclear magnetic resonance and elastic wave velocity measurements. *J. Appl. Geophys.* **2016**, *127*, 68–81.
35. Ge, X.; Fan, Y.; Zhu, X.; Chen, Y.; Li, R. Determination of nuclear magnetic resonance T_2 cutoff value based on multifractal theory—An application in sandstone with complex pore structure. *Geophysics* **2015**, *80*, D11–D21.
36. Dong, J.; Huang, Z.; Chen, J.; Zhang, W.; Wang, L.; Li, T.; Huang, Q.; Liu, L. A new method to establish NMR T_2 spectrum based on bimodal Gaussian density function: A case study of tight sandstone in East China Sea Basin. *J. Pet. Sci. Eng.* **2018**, *167*, 628–637.
37. Kulesza, S.; Bramowicz, M. A comparative study of correlation methods for determination of fractal parameters in surface characterization. *Appl. Surf. Sci.* **2014**, *293*, 196–201. [[CrossRef](#)]
38. Cai, J.; Wei, W.; Hu, X.; Wood, D.A. Electrical conductivity models in saturated porous media: A review. *Earth Sci. Rev.* **2017**, *171*, 419–433.
39. Pfeifer, P.; Avnir, D. Chemistry in no integral dimensions between two and three: I. Fractal theory of heterogeneous surfaces. *J. Chem. Phys.* **1982**, *79*, 3369–3558.
40. Zhang, Z.; Weller, A. Fractal dimension of pore-space geometry of an Eocene sandstone formation. *Geophysics* **2014**, *79*, D377–D387.
41. Rezaee, R.; Saedi, A.; Clennell, B. Tight gas sands permeability estimation from mercury injection capillary pressure and nuclear magnetic resonance data. *J. Pet. Sci. Eng.* **2012**, *88*, 92–99.
42. Dillinger, A.; Esteban, L. Experimental evaluation of reservoir quality in Mesozoic formations of the Perth Basin (Western Australia) by using a laboratory low field Nuclear Magnetic Resonance. *Mar. Pet. Geol.* **2014**, *57*, 455–469.
43. Wang, Z.; Pan, M.; Shi, Y.; Liu, L.; Xiong, F.; Qin, Z. Fractal analysis of Donghetang sandstones using NMR measurements. *Energy Fuels* **2018**, *32*, 2973–2982. [[CrossRef](#)]
44. Conlon, P.A.; Gallagher, P.T.; McAteer, R.T.J.; Ireland, J.; Young, C.A.; Kestener, P.; Hewett, R.J.; Maguire, K. Multifractal properties of evolving active regions. *Sol. Phys.* **2009**, *248*, 87–99.
45. Shao, X.; Pang, X.; Li, H.; Zhang, X. Fractal analysis of pore network in tight gas sandstones using NMR method: A case study from the Ordos Basin, China. *Energy Fuels* **2017**, *31*, 10358–10368.
46. Tavakoli, V.; Rahimpour-Bonab, H.; Esrafil-Dizaji, B. Diagenetic controlled reservoir quality of South Pars gas field, an integrated approach. *Comptes Rendus Géoscience* **2011**, *343*, 55–71. [[CrossRef](#)]

Disclaimer/Publisher’s Note: The statements, opinions and data contained in all publications are solely those of the individual author(s) and contributor(s) and not of MDPI and/or the editor(s). MDPI and/or the editor(s) disclaim responsibility for any injury to people or property resulting from any ideas, methods, instructions or products referred to in the content.